Low-THz Transmission Through Water-Containing Contaminants on Antenna Radome

Norouzian, Fatemeh; Du, Rui; Hoare, Edward; Gardner, Peter; Constantinou, Costas; Cherniakov, Mikhail; Gashinova, Marina

DOI:
10.1109/TTHZ.2017.2778498

Low-THz Transmission Through Water-Containing Contaminants on Antenna Radome

Fatemeh Norouzian, Rui Du, Edward G. Hoare, *Senior Member, IEEE*, Peter Gardner, Costas Constantinou, Mikhail Cherniakov, and Marina Gashinova

***Abstract*—In this paper, signal reduction due to the presence of water content formed on a radome has been studied at low-THz frequencies. The effect of obscurants on signal reduction has been characterized by measuring the ratio of reflected signals from a reference target through the radome, with contaminant and without contaminant. All the measurements have been compared to theoretical models, demonstrating a reasonable agreement. Water is the most common obscurant in outdoor applications and the main cause of performance deterioration in rainy, snowy, and foggy weather. This paper concentrates on the attenuation caused by different forms of distribution of water as a radome contaminant. Both a thin uniform layer of water and randomly distributed water droplets are studied at 150 and 300 GHz. The results show strong signal reduction due to the presence of uniform thickness of water and higher signal reduction with increasing frequency. However, the measured transmissivity through distributed water droplets, which occur in practice due to the surface tension of water, shows lower transmission loss at the shorter wavelength, due to transmission through the distribution of gaps between droplets.**

***Index Terms*—Diffraction, loss measurement, refractive index, submillimeter-wave propagation.**

I. Introduction

TECHNOLOGICAL advances, which help to improve safety and comfort for all road users and increase the efficiency of cars on the road, have attracted significant attention over the last few decades. According to the European Commission [1], in 2014, 26 000 fatalities have been reported due to car accidents in Europe. A study on identifying the cause of road crashes in Europe [2] shows the main cause of road accidents to be human error. Advanced driver assistance systems (ADAS) and car autonomy have the potential to improve safety and comfort to road users. ADAS informs the driver or provides active assistance by recognition, tracking and avoidance of any potential hazards, and identifying the road surface. There are different sensor technologies for driver assistance systems, such as light detection and ranging (LIDAR), microwave radar, and optical cameras [3], [4]. LIDAR uses infrared and is able to detect small objects; however its performance suffers in nontransparent media, which can be expected in outdoor environments. Optical cameras are cheap, light, and produce an image of a high resolution. Cameras are highly susceptible to most types of contaminant, obscurants in the air, and changes in the lighting conditions. Automotive sensors need to be robust under a wide range of environmental and weather conditions to provide partial or full autonomy. LIDARs and optical cameras are unable to fulfill this requirement. Radar can provide an advantage of robust operation in all weather conditions and in any lighting condition.

Current automotive radars that operate at 24 and 77 GHz, if used for imaging would deliver low image resolution compared to optical sensors. Reduction of antenna size is another key requirement for automotive applications due to already dense in-vehicle packaging, and if achieved, this will result in lower integration costs. Therefore, there is a need for new sensing systems that fulfill the entire range of requirements for LIDAR, radar, and camera systems. Low-terahertz (THz) spectrum refers to the portion of electromagnetic spectrum from 0.1 to 1 THz. At this frequency range, an antenna aperture size is expected to be very small, which is a big advantage for automotive applications. Wide operational bandwidth, achievable at low-THz bands, results in high image resolution, approaching that of electro-optical sensor imagery.

Low-THz radar has found many applications in indoor environments. One of the most successful applications of THz radiation is imaging, which has been used in different areas such as biomedical [5], security [6], [7], and more recently automotive applications [8]. The high fingerprint spectra of materials in low-THz range have also facilitated an application in material characterization in this frequency band [9]. The ability to provide high operational bandwidth at low-THz bands made this region of the spectrum attractive for high-bandwidth communications [10]. Until now, all proposed low-THz applications have focused on indoor environments. Thus, the influence of the harsh outdoor environment on the performance of the low-THz sensors remains largely unknown. This lack of knowledge results in the requirement for a thorough study to prove the feasibility of using low-THz frequencies for sensing in uncontrolled environmental conditions. However, automotive radars operate at a range of up to 200 m and the specific attenuation of less than 10 dB/km for the frequency range of 0.1–0.3 THz reported in [11] corresponds to a two-way excess path loss of less than

Manuscript received March 6, 2017; revised September 20, 2017; accepted November 14, 2017. Date of publication December 22, 2017; date of current version January 9, 2018. This work was supported by the Engineering and Physical Sciences Research Council under the TRAVEL project EP/L019078/1. *(Corresponding author: Fatemeh Norouzian.)*

The authors are with the Department of Electronic, Electrical, and Systems Engineering, University of Birmingham, Birmingham B15 2TT, U.K. (e-mail: f.norouzian@bham.ac.uk; RXD550@student.bham.ac.uk; e.g.hoare@bham.ac.uk; p.gardner@bham.ac.uk; c.constantinou@bham.ac.uk; m.cherniakov@bham.ac.uk; m.s.gashinova@bham.ac.uk).

Color versions of one or more of the figures in this paper are available online at http://ieeexplore.ieee.org.

Digital Object Identifier 10.1109/TTHZ.2017.2778498

4 dB, which is not a significant issue in terms of system design and operation.

We are investigating the performance of low-THz sensors in terms of transmissivity in the presence of different radome contaminants (mud, oil, grit, etc.) and various weather conditions (rain, snow, fog, etc.). The presence of water on the radome and in the atmosphere is one of the main reasons for the reduction in performance of automotive sensors in adverse weather conditions. The reduction of signal in the presence of pure water and contaminated water with salt and road dirt in the propagation path is the subject of this contribution.

The deleterious effects on the propagation characteristics of water built up on the radome of the antenna, and the presence of water droplets in the atmosphere, have been topics for research over the last few decades [12]–[18]. In [12], the propagation losses for varying precipitation rates have been measured at 94 GHz over two years and excess attenuation of 9–14 dB has been reported for wet antennas. In [14], transmission loss of 20 dB is measured when the radome water thickness is approximately 1.5 mm at 20 GHz. A theoretical model of reflection and transmission through water films on the radome at 24, 76.5, and 140 GHz was presented in [15]. The simulation results at 76.5 GHz were compared with measurement results and showed a loss of about 30 dB for a 1-mm-thick water layer. Attenuation of near infrared radiation through water film with average thicknesses between 100 and 380 μm has been measured in [16] and the results confirm the presence of strong attenuation even with a very thin layer of water.

This paper is structured as follows. In Section II, transmission loss due to the presence of a uniform thickness of pure water and water with different contaminants (salt and road dirt) in the propagation medium is measured at two low-THz frequencies (150 and 300 GHz) and the experimental results are compared to theoretical predictions. Also, an estimation of the permittivity of pure and contaminated water from the measured transmission coefficient is discussed in this section. Section III studies the effect of a random distribution of water droplets on the radome based on diffraction theory, and then measurement results are compared with the theoretical results. Conclusions and a discussion of future work are finally presented in Section IV.

II. Effect of Uniform Thickness of Water Formed on Radome

The aim of this section is to determine transmission loss due to the presence of uniform thickness of water at 150 and 300 GHz by both theoretical modeling and measurement. Permittivity is an important parameter to predict transmission behavior theoretically. A lack of reliable empirical data for the permittivity of pure and contaminated water at low-THz frequencies gives rise to a requirement to study this parameter at these frequencies.

A. Analytical Approach

A theoretical model based on Fresnel theory [19] of reflection and transmission for multilayer structures is adopted. The model is developed for a three-layer structure, air–water–air, which is shown in Fig. 1. The complex refractive index of a material $\tilde{n}(f,T) = n' - jn''$, which depends on both frequency and temperature, will result in reflection (R_1) of some of the energy at the first medium interface. The rest of the energy will be transmitted through the second medium (T_1). Again, at the second interface, some of the energy will be reflected (R_2) and the rest of the energy will be transmitted to the third medium (T_2). The reflection and transmission coefficients of each sample are different and depend on the permittivity, thickness, and shape of the sample.

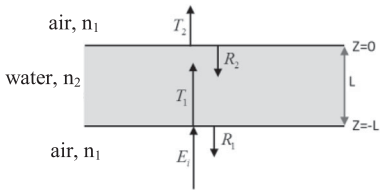

Fig. 1. Three-layer structure used in the modeling of uniform layer of water. Refractive index of air and water are shown by n_1 and n_2, respectively.

The radome is placed in the far field of the antennas and the assumption of plane wave incidence is made. To characterize the effect of a uniform thickness of water on the transmissivity of the signal, the reflection coefficient in the first medium (R_1) and the transmission coefficient in the third medium (T_2) need to be studied and they can be calculated by

$$R_1 = \frac{\eta_{\text{in}} - \eta_0}{\eta_{\text{in}} + \eta_0} \tag{1}$$

$$T_2 = \frac{2\eta_0}{\eta_{\text{in}} + \eta_0} \tag{2}$$

where η_{in} is the input impedance at $Z = -L$ and η_0 is the wave impedance of the first medium (air). η_{in} can be calculated using transmission line theory as follows:

$$\eta_{\text{in}} = \eta_1 \frac{\eta_0 \cosh(\beta_2 L) + \eta_1 \sinh(\beta_2 L)}{\eta_1 \cosh(\beta_2 L) + \eta_0 \sinh(\beta_2 L)} \tag{3}$$

where L is the thickness of water and β_2 is the complex wavenumber in the second medium. The characteristic impedances of water (η_1) is calculated by $\sqrt{j\omega\mu/(\sigma + j\omega\varepsilon)}$, where μ is a permeability, σ is a conductivity, and ε is a permittivity of the medium. The complex permittivity of water has been calculated using the "double Debye" model [20]

$$\varepsilon_r(f) = \varepsilon_\infty + \frac{\varepsilon_S - \varepsilon_1}{1 + j\omega\tau_1} + \frac{\varepsilon_1 - \varepsilon_\infty}{1 + j\omega\tau_2} \tag{4}$$

where ε_s, ε_∞, and ε_1 are the static dielectric constant, the dielectric constant at the high-frequency limit, and an intermediate dielectric constant, respectively. τ_1 and τ_2 are the first and second Debye relaxation times [20]. The literature does not provide consistent values for these parameters. The values in this paper are taken from the works in [20]–[25]. The first and second Debye relaxation times are reported between 8.2–9.6 ps and 0.17–1.2 ps, respectively. Values between 4.93 and 6.53 have been reported for ε_1 and between 3.3 and 4.4 for $\varepsilon_{\mathbb{E}}$. Therefore, the real (ε_r') and imaginary (ε_r'') parts of the permittivity of water at 150 GHz (f_1) and 300 GHz (f_2) are obtained as

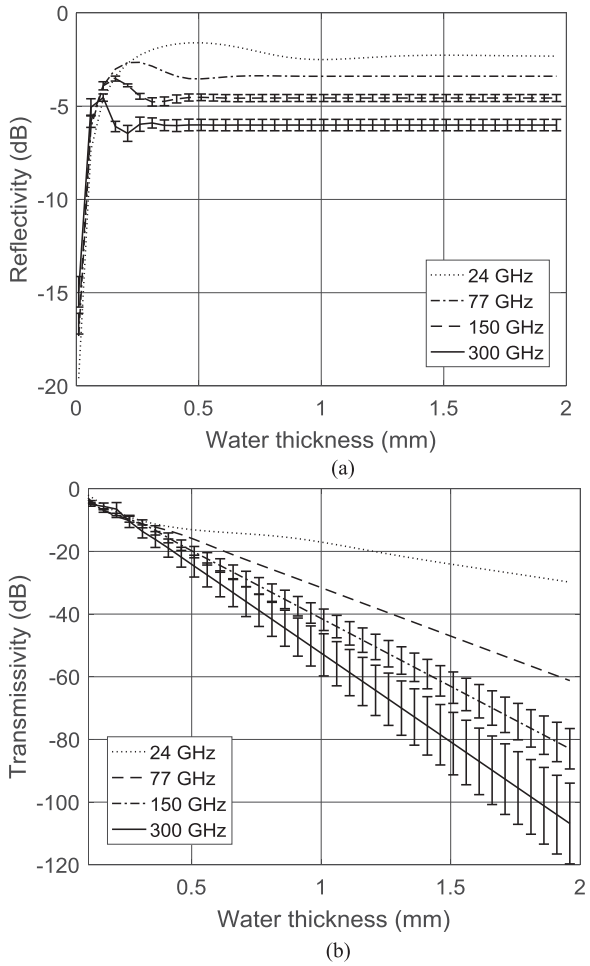

Fig. 2. Calculated (a) reflectivity and (b) transmissivity of pure water film as a function of water thickness at 24 GHz, 77 GHz, 150 GHz, and 300 GHz at 23 °C. The error bars correspond to the uncertainty in the double Debye model parameters in (4).

follows:

$$\varepsilon'_r(f_1) = 4.92 - 7.65 \qquad \varepsilon''_r(f_1) = 8.1 - 10.75$$
$$\varepsilon'_r(f_2) = 3.8 - 6.6 \qquad \varepsilon''_r(f_2) = 4.19 - 6.23$$

For an initial approximation of reflectivity and transmissivity of water, the permittivity of water has been calculated based on the values of 8.5 ps, 1 ps, 6, and 4.4 for τ_1, τ_2, ε_1, and ε_{∞}, respectively. These values yield $\varepsilon_r(f_1) = 6.3 - j9.6$ and $\varepsilon_r(f_2) = 5 - j5.1$. The simulated results for reflectivity and transmissivity at four frequencies, two current automotive frequencies (24 and 77 GHz) and two low-THz frequencies (150 and 300 GHz) are plotted in Fig. 2. Permittivity values of pure water at 24 GHz and 77 GHz are found in [24] and [26], respectively.

Reflection from pure water [see Fig. 2(a)] increases with the water thickness and it reaches its maximum at a thickness that is dependent on the wavelength. Then, it stays constant for higher thicknesses as most of the energy will be absorbed and all internal reflections will be negligible; therefore, reflectivity does not change for higher thickness. Fig. 2(b) illustrates that the transmitted signal attenuation for 24 GHz, 77 GHz, 150 GHz, and 300 GHz reaches about 30 dB, 61 dB, 94 dB, and 108 dB in 2-mm uniform water layer, respectively. However, for water layer thickness below 0.6 mm, the difference in transmission attenuation between 77 GHz and low-THz frequencies is only about 10 dB. Even though water of greater thickness can accumulate on a radome for short periods of time, the air flow due to the movement of the vehicle thins the water layer to typically submillimeter thicknesses.

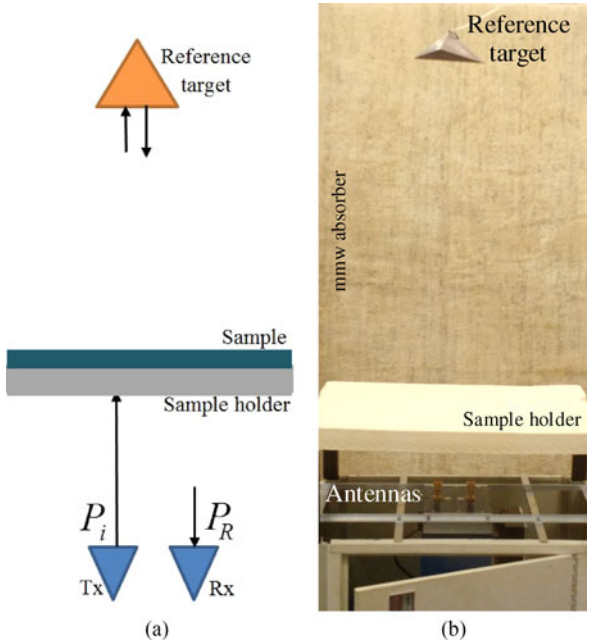

Fig. 3. Measurement setup configuration (a) general view and (b) actual setup.

B. Measurement Methodology

The measurement methodology is based on the direct implementation of the radar principle, i.e., considering explicitly the ratio of the signal strength reflected from a reference target through the radome without obstructing the signal received at normal incidence through a radome covered by a contaminant.

The measurement setup is shown in Fig. 3. The quasi-monostatic radar consisting of collocated transmit and receive antennas is positioned vertically and is pointing upwards. The transmit and receive signals are shown by P_i and P_R in Fig. 3(a), respectively. A reference target with a known radar cross section (RCS) is suspended above the antennas. A trihedral corner reflector is chosen as a reference target with a RCS of 29.4 dBsm at 300 GHz. A sample of contaminant is placed between the antennas and the reference target in the path of the signal. This requires having a sample holder that is sufficiently rigid to provide a stable and robust platform that does not sag under the weight of the sample and is replaceable after each measurement. Other important characteristics for the sample holder are low reflection and low attenuation of the signal that require having a thickness equal to an integer of half-wavelength, low refractive index, and low loss tangent. Closed cell polyurethane foam that has a thickness of 50 mm and a dielectric constant of approximately 1.2 with low dissipation factor (a value under

0.005 is given by the manufacturers for microwave frequencies) is chosen as a radome prototype and placed perpendicular to the direction of propagation. Samples are placed on the sample holder in such a way as to obscure the radar beam. The area that the sample needs to cover should be greater than the footprint of the illuminating beam, defined by the 3-dB roll-off of the radiation pattern, to guarantee that most of the energy passes through the sample. According to the distance between the sample holder and antennas (200 mm) and also the beamwidth of the antennas (azimuth and elevation angle of 10°), the sample must cover an area exceeding 35 mm × 35 mm. The advantage of this setup is that different samples can be introduced without requiring further alignment.

The signal reduction that occurs due to the presence of the sample is a combination of various phenomena such as: reflection, refraction, and absorption. It is labeled as *"Transmissivity,"* and can be calculated by

$$T(\text{dB}) = 10\log\left(\frac{P_R}{P_{R0}}\right) \tag{5}$$

where P_R and P_{R0} are the reflected power from the reference target through the radome covered by a sample and through the radome without a sample (reference signal), respectively.

The measurements were conducted using two radar systems: a frequency-modulated continuous-wave radar with a frequency sweep of 144–150 GHz and a stepped frequency radar (SFR) with the frequency sweep of 282–298 GHz. The SFR is a system based on an Agilent FieldFox portable vector network analyzer with VivaTech [27] upconverter (transmit) and downconverter (receive). The RF input of the upconverter spans a frequency of 2–18 GHz and the corresponding frequency of the RF input of the downconverter is 282–298 GHz.

One of the challenges in this measurement is to provide a quantifiable thin uniform layer of water due to the adhesion and surface tension properties of water. A known volume of water is deposited on tissue paper with a known shape and area; therefore, the thickness of the uniform water layer resulting from the wetting of the tissue can be readily calculated. This technique gives ability to provide a uniform layer of water with accuracy of 0.05 mm. In order to produce a thicker layer of water, several tissue papers are stacked together. All the measurements in this paper are done for a number of realizations. The results have proved that the technique provides the required repeatability as the coefficient of variation (C_v) is smaller than 1, $-1<\sigma/\mu<1$. Possible errors in this measurement setup arise due to presence of small air gaps between the tissue papers and the nonuniform density of the tissue paper itself.

C. Measurement Results

In this section, the results of measured transmissivity through uniform layer of pure water and contaminated water with salt and road dirt are presented. Also, because of the inconsistency and unavailability of the reported values for permittivity of water, the permittivity of pure and saline water has been calculated from the measured transmission through a uniform layer.

1) Pure Water: There are several experimental methods to calculate the relative dielectric permittivity of material [28]. In this paper, the free-space technique has been chosen that enables the calculation of the complex permittivity from measured reflection and transmission coefficients. The calculation can use either the reflection or the transmission coefficient or both of them. However, use of the transmission coefficient is more practical for calculation of permittivity at high frequencies, as the reflection coefficient measurements are sensitive to surface roughness. The explicit derivation of the complex permittivity for lossy materials from just the transmission coefficient is not viable. However, the complex permittivity can be estimated through a root searching procedure that minimizes the estimation error between theory and measurement, constrained by the range of reported complex permittivity values for pure water

$$D\left(\varepsilon'_r, \varepsilon''_r\right) = \sum_{i=1}^{N} \left|T_m\left(f, t_i\right) - T_t\left(f, t_i, \varepsilon'_r, \varepsilon''_r\right)\right| \tag{6}$$

where T_m and T_t are the measured and calculated transmission coefficients, respectively; the thickness of the water layer is denoted by *t*. Values of *D* for various combinations of ε' and ε" are shown in Fig. 4. The minimum estimation error in the defined boundaries (based on the reported permittivity in the literatures) has been found for values of $\varepsilon_r(f_1) = 7 - j10$ and $\varepsilon_r(f_2) = 4.5 - j4.8$.

The measured and calculated transmissivities of pure water at both frequencies with the obtained permittivities are plotted in Fig. 5 showing an excellent agreement between the calculated and measured results. The small discrepancies observed are likely to arise due to the factors mentioned earlier, such as the presence of air gaps and slight nonuniformity of the water layer, as well as the expected process of water evaporation during multiple measurements, which will change the true thickness of the water layer.

The measurement points and $\pm\sigma$ error bars shown in all experimental figures herein are the results obtained from ten independent measurements on two or more sample realizations. Generally, transmission through pure water decreases rapidly as the thickness of the water film increases. The trend of transmissivity through pure water at 300 GHz has a steeper slope than that seen in the 150-GHz results. The transmissivity of water at 150 GHz and 300 GHz are shown up to a water layer thickness of 0.6 mm and 0.45 mm, respectively, as above that is outside of our dynamic range.

2) Water Contaminated With Salt: Results of a study on transmissivity through water of different levels of salinity are presented in this section. Analysis of the effect of water salinity on millimeter-wave propagation is undertaken in this paper, as this will represent two important use cases: driving in winter conditions and a car being in coastal areas. Indeed, we can expect that the salt deposited on a radome of the automotive sensor in the coastal areas may become so thick that it may entirely block the signal. In addition, grit with a high concentration of salt is usually spread on roads during autumn–winter periods,

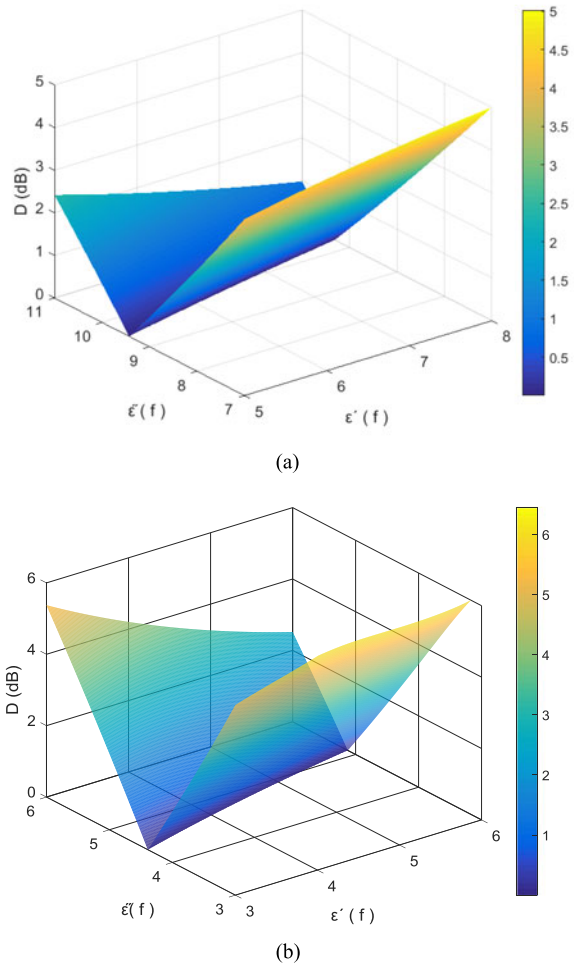

Fig. 4. Deviation between calculated and measured transmissivity at (a) 150 GHz and (b) 300 GHz.

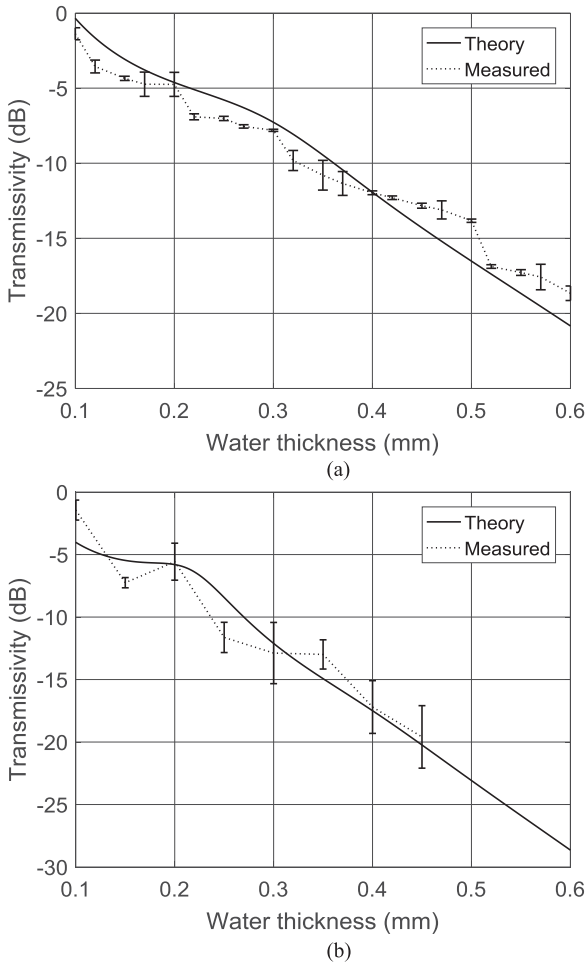

Fig. 5. Calculated and measured transmissivity of pure water film as a function of water thickness at (a) 150 GHz and (b) 300 GHz at 23 °C.

and such particulates build up on a radome may cause similar effects.

Water contaminated with salt was produced in the laboratory to simulate seawater. The salinity of seawater is defined in grams of salt per kilogram of solution (g/kg), which is called the practical salinity unit (PSU). The salinity of water can also be shown by a percentage figure (%), where 10 PSU is equal to 1%. Seawater salinity is predominantly approximately between 32 and 37 PSU, as seawater is not uniformly saline throughout the world [29]. So, three salinities have been chosen (31, 35, and 38 PSU) as samples to investigate how the salinity of water deposited on a radome affects the signal reduction of low-THz waves. Natural seawater from the Aegean Sea was also used in the experiment for comparison. The results of transmissivity through uniform layer of salty water with respect to different layer thickness are shown in Fig. 6 for both frequencies.

Similar to the results for pure water, transmission decreases with increase of water film thickness. The dependence of the transmissivity on salinity is not clear, as it does not exhibit a monotonic trend to draw a strong conclusion. The transmissivity through the sample of water from the Aegean Sea lies between the produced solutions.

There is little information in the literature on the permittivity of seawater at low-THz frequencies, as mentioned earlier. The permittivity of seawater has been measured up to 90 GHz in [26]. Permittivities of salt water with different concentrations of 0.1, 1.0, and 3.5 mol/L have been measured up to 3 THz in [30]. Finally, permittivity of 2-mol/L NaCl up to 1 THz has been measured in [31]. Molarity of seawater is approximately between 0.5 and 0.7 mol/L (molarity (M) = PSU/58.45). The permittivity of solutions with the molarity in this range at our working frequencies is missing in the literature. We can estimate the permittivity of seawater by using (6) as explained in Section II-C1. The calculated permittivity for three different salinity levels and seawater are shown in Table I. The measured and calculated transmissivities (with the obtained permittivity) through a water film with salinity of 3.5% is plotted in Fig. 7 for both frequencies.

3) Water Contaminated With Road Dirt: Splashing of water from a wet road is very common on rainy days and the performance of the sensor when splashed water covers the radome is investigated and discussed in this section. Road water contains particulates: small airborne exhaust particles, dust, sand, etc. In [31], the transmission loss in a uniform water layers build up on the radome in different rain intensity has been measured on

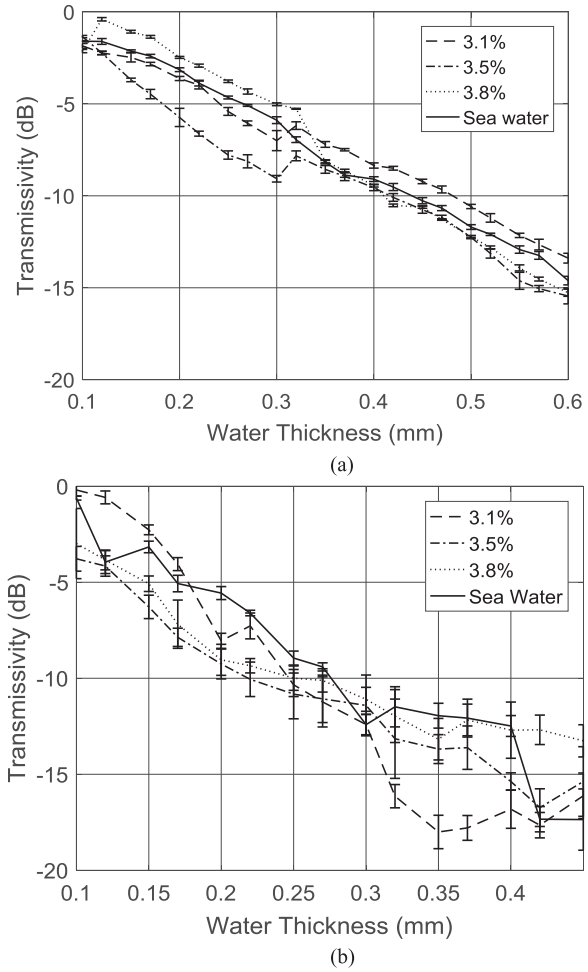

Fig. 6. Measured transmissivity through water of three different salinities and the actual seawater as a function of water thickness at 23 °C (a) at 150 GHz and (b) at 300 GHz.

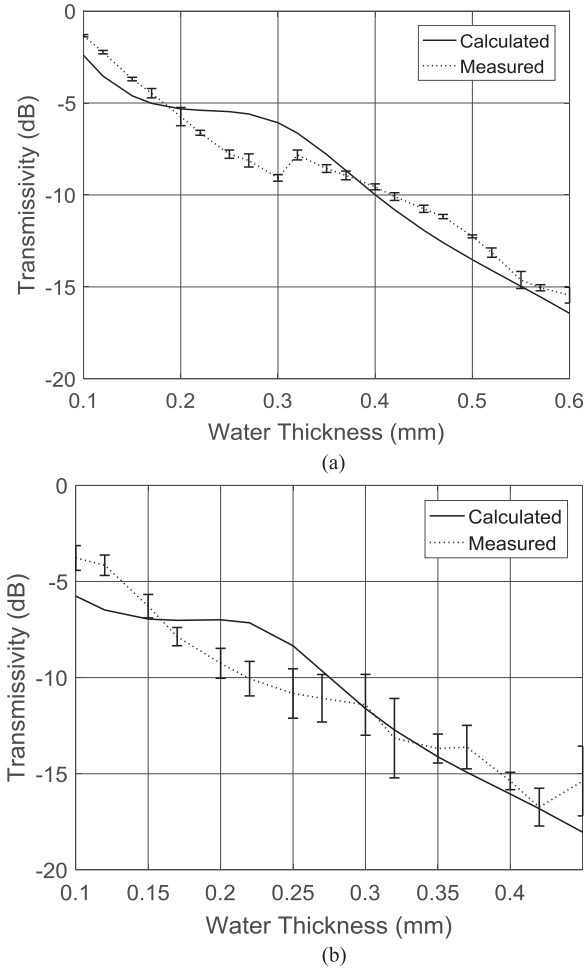

Fig. 7. Calculated and measured transmissivity through a film of water contaminated with salt, with salinity of 3.5% as a function of uniform thickness at (a) 150 GHz and (b) 300 GHz at 23 °C.

TABLE I
CALCULATED PERMITTIVITY OF SALINE SOLUTIONS AT 150 AND 300 GHz

Salinity	150 GHz		300 GHz	
	ε'_r	ε''_r	ε'_r	ε''_r
3.1%	8.8	6.28	4.46	3.57
3.5%	8.25	7.27	4.23	3.53
3.8%	8.25	7.27	4.23	3.53
Seawater	8.32	6.5	4.54	3.1

dirty, clean, and waxed radomes for C-band weather radar. It has been concluded that the difference between clean and dirty radomes is negligible, whereas waxed radomes present an additional transmissivity of about 1 dB. For low-THz frequencies, a similar study of this sort is altogether missing.

The contaminated water with road dirt was collected from a puddle in the road on a raining day. This water was heavily contaminated with soil, dust, and airborne particles. The transmissivity through water with road dirt versus water film thickness is shown in Fig. 8.

Measurement results shown in Fig. 8 illustrate a decrease in transmissivity with increasing water layer thickness for both frequencies. The transmissivity of pure water and heavily contaminated water with road dirt shows similar performance and the difference between them can be explained by scattering from particles in contaminated water. The transmissivity of pure water is higher than that of water contaminated with road dirt at 150 GHz, but this observation reverses at 300 GHz. This is potentially due to the fact that we have no control over the homogenous depositing of the dirt on the tissue paper, which is a plausible explanation for the substantially increased size of the error bars in Fig. 8(b). Additionally, we have used different dirty water samples for the two measurements that introduce a further uncontrolled source of variability in such a comparison. As a detailed analysis of the dielectric properties of road dirt solutions is not available (or meaningful since it is not controllably repeatable), these results are indicative rather than definitive.

III. EFFECT OF WATER DROPLETS FORMED ON RADOME

In most of the real-life scenarios in moderately wet weather, a water layer of uniform thickness does not form on the radome

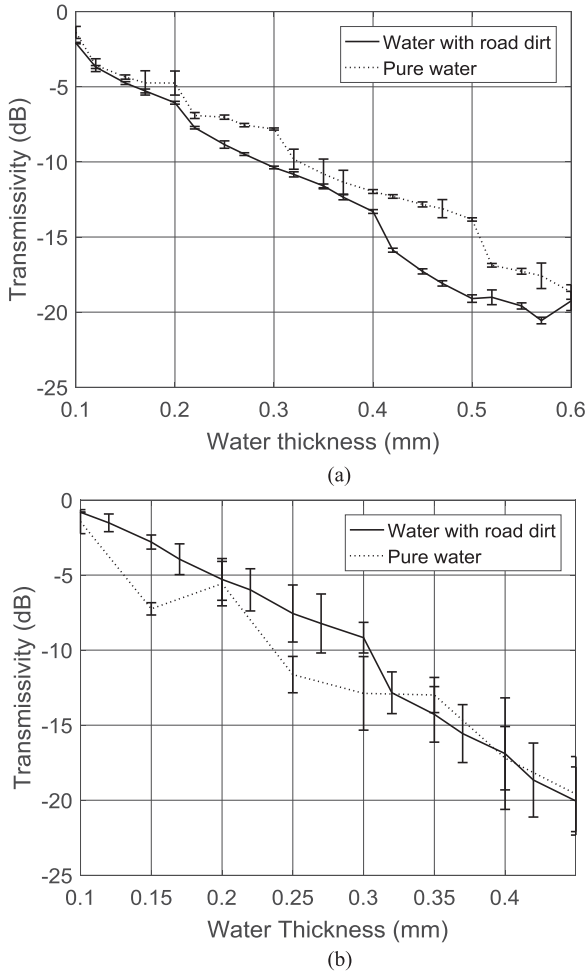

Fig. 8. Measured transmissivity of contaminated water from a road puddle and pure water as a function of water layer thickness at 23 °C (a) at 150 GHz and (b) at 300 GHz.

due to the adhesion properties of water. The build up of water on the radome in outdoor scenarios typically leads to randomly distributed water droplets. The aim of this section is to quantify the reduction in intensity of low-THz waves through a screen of randomly distributed water droplets.

A. Analytical Approach

Wave propagation through a screen comprising water droplets of a range of arbitrary sizes and a random spatial distribution is a complicated modeling problem. Water droplets normally have hemispherical shape and the scattering mechanisms of a hemispherical particle are depicted in Fig. 9. Reflection is shown as specular reflection and diffraction is shown as a creeping wave that travels along the curved surface.

To build a model of wave propagation through a screen of randomly distributed water droplets, knowledge of the droplets' size distribution is necessary. The size of droplets generated by spray on the surface has been measured with "Alicona Infinite-Focus," which is an optical three-dimensional measurement device based on focus-variation technology [33]. This technology provides the topographical and color information based on the

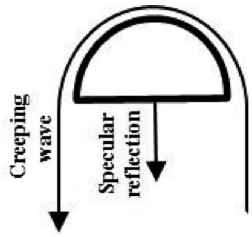

Fig. 9. Scattering mechanism of a hemisphere particle.

variation of focus of an optical system with vertical scanning. The results indicate that droplets have diameters between 1 and 6 mm and thickness between 0.5 and 3 mm in their center. The spaces between droplets are also measured for a few realizations and it shows an average of 10-mm spaces between droplets.

Hulst proposed criteria to characterize the applicability of theoretical scattering models used to study the transmission through particles based on their size [34]. These areas are defined by parameter *M*, which relates the size of the particle to the wavelength (λ) in the material of particle

$$M = \frac{2\pi r n}{\lambda} \tag{7}$$

where *r* is radius and *n* is the refractive index of the particle. The scattering theories and their domain of applicability are as follows:

$$\begin{aligned} M &\ll 1 \quad \text{Rayleigh scattering region} \\ M &\approx 1 \quad \text{Mie scattering region} \\ M &\gg 1 \quad \text{Optical scattering region} \end{aligned} \tag{8}$$

By substituting the size of the smallest obstacle in our scenario and the value of measured refractive index presented in Section II, we can see that $M > 1$ so that the scattering regime is predominantly optical and, therefore, we can use diffraction theory for the modeling. Based on the results of Section II, almost all the wave has been absorbed (signal reduction of 20 dB) after travelling through a water path of length more than 0.5 mm at both frequencies. Therefore, an assumption can be made that the wave amplitude transmitted through the water droplets is negligible and they can be considered as fully blocking "screens," implying in turn that the entire transmitted wave will propagate through the gaps between droplets. In this approximation, the projected area of the droplets is important, but their volume and internal scattering arising inside the droplets are not considered. Naturally, this simple model introduces some error, as the droplets do not have uniform thickness; they are thinner near their edge (which can give rise to some transmitted energy). The simplest theory that can explain the transmission of the low-THz wave through the gaps between droplets is Kirchhoff's diffraction theory [35].

The scenario under study is depicted in Fig. 10. The source point is P_0 and *P* is the observation point. They are located at $(0, 0, -d_0)$ and $(0, 0, d)$, respectively. The particle screen that consists of randomly distributed droplets is placed between the source and the observation point. As mentioned earlier, the volume of the droplets is not considered in this model and the

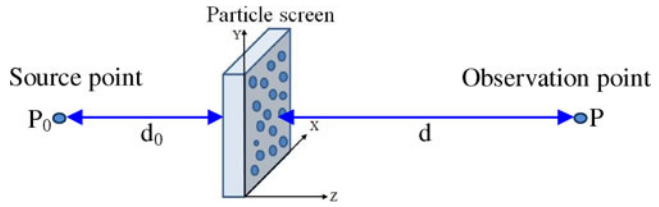

Fig. 10. Random droplet model.

opaque particle screen is thus considered to be two dimensional. The important model parameters are as follows:

1) the size of the droplets (diameter);
2) the size of the gaps between droplets;
3) the distance between the center of each gap and the source point; and
4) the distance between the center of each gap and the observation point.

If droplets and gaps called *A* and *B,* respectively (the gap is the distance from the edge of one droplet to the edge of its nearest neighbor droplet), and to simplify the problem, the wave *amplitude transmission coefficient* on the plane $z = 0$ is considered to be zero for the droplets and unity for the gaps

$$A \Rightarrow U = 0$$

$$B \Rightarrow U = 1$$

The power at the observation point when the signal propagates through the particle screen can be calculated using Kirchhoff's diffraction theory [35]

$$I_P = -\frac{j\alpha k}{8\pi^2} \int_S \left(\frac{\exp(jkr)}{r}\right) \cdot \left(\frac{\exp(jkR)}{R}\right) dS \quad (9)$$

where α is the isotropic source power, *S* is the total clear area of the screen (combined gaps), and *k* is the wavenumber. The distances from the screen to the source point and to the observation point are shown by *r* and *R,* respectively. The particle screen can be represented by a matrix of $N \times M$ with elements equal to 1 or 0, where 1 represents the gap between particles and 0 represents the particles. Therefore, Kirchhoff's diffraction is discretized by replacing the integral with a summation to rewrite (9) as

$$I_P = -\frac{j\alpha k}{8\pi^2} dM \sum_{n=1}^{N} \sum_{m=1}^{M} \left(\frac{\exp(jkr_{n,m})}{r_{n,m}}\right) \cdot \left(\frac{\exp(jkR_{n,m})}{R_{n,m}}\right) \quad (10)$$

where *n* and *m* are the coordinates of each gap in the matrix and *dM* is the area assigned to each element of the matrix. The distance between each element of the matrix and the source point and the observation point are shown by $r_{n,m}$ and $R_{n,m}$, which can be calculated by $r_{n,m} = \sqrt{d_0^2 + {x_n}^2 + {y_m}^2}$ and $R_{n,m} = \sqrt{d^2 + {x_n}^2 + {y_m}^2}$, respectively. In our modeling, we have chosen the particle screen to be a square of 10 cm $\times$ 10 cm. Therefore, a physical dimension can be allocated to each element of the matrix (*dM*). Therefore, *x* and *y,* which are the distance of each mesh to the center of the screen, can be calculated by counting the number of elements between the specific element and the center element of the matrix and multiplying them by *dM*. The study of the propagation through a screen covered by droplets has started with producing matrices in MATLAB that include random size and distribution of particles with log-normal size distribution (fitted distribution with the measured sizes of droplets and spaces is shown in Section III-B). The discrete form of Kirchhoff's diffraction theory (10) is applied to calculate the transmitted field intensity through the corresponding screen. To understand the effect of the gap dimensions on the wave propagation, particle screens with different gap sizes have been produced with the minimum and average gaps sizes as follows:

1) minimum gap = λ/4, mean gap = λ;
2) minimum gap = λ, mean gap = 4λ;
3) minimum gap = 2λ, mean gap = 7λ;
4) minimum gap = 4λ, mean gap = 13λ.

The graph in Fig. 11 depicts the average transmissivity through four produced randomly distributed droplets screens. The *x*-axis shows the area covered by droplets by percentage, which starts from about 0% and finishes about 80%. The average standard deviations of transmissivity for each point for all the four plots are smaller than 0.01. As can be seen in Fig. 11, the trend of the transmissivity when the average spacing between droplets takes the values λ and 4λ is decreasing when the area covered by particles is increasing. When the average spacing exceeds 4λ, the initial trend in transmissivity is around 0 dB with occasional positive values (transmissivity enhancement, albeit

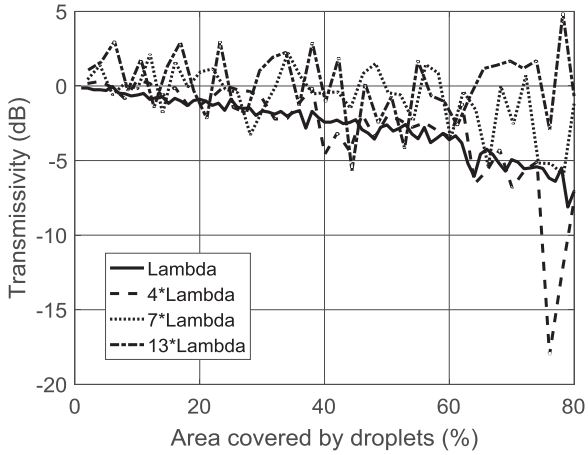

Fig. 11. Transmissivity through the produced randomly distributed droplets for four average sizes of gaps.

Fig. 12. Black and white image of a droplet screen realized experimentally

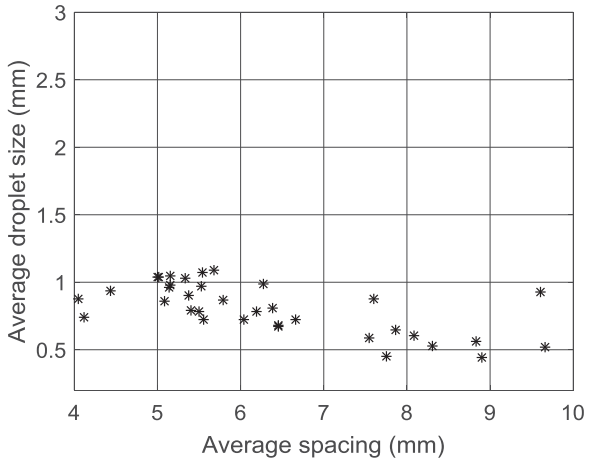

Fig. 13. Average droplet size versus average spacing between droplets.

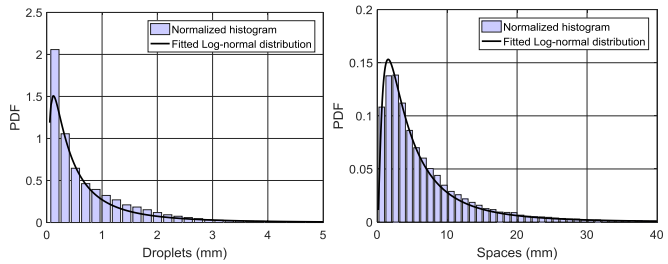

Fig. 14. Fitted distribution and histogram of droplets and spaces.

TABLE II
GEOMETRICAL PARAMETERS DISTRIBUTION

	Minimum	Average	Maximum
Spaces	0.16 mm	7.4 mm	100 mm
Droplets	0.05 mm	0.8 mm	22.3 mm

in only one spatial direction) for coverage less than 60%. When gaps have electrical dimension larger than the wavelength, the transmissivity through the screen is approximately 0 dB. This is favorable for low-THz outdoor applications, as this requirement is achievable with very short wavelength signals.

B. Measurement Methodology

The measurement setup (the position of the radar, the sample holder, and the reference target) is as described in Section II-B. To simulate water built-up on a radome, 1 mm^3 of water has been sprayed on the sample holder for 40 times. The measurement of transmissivity through a radome with water droplets on it started with characterizing the size distribution of water droplets on the radome. Fig 12 shows the black and white image of typical water droplets distribution, as an example. The area coverage by droplets in this figure is 12.3%. The captured optical photograph is transformed in a binary image, so that it represents an array of clustered ones and zeros. By counting the number of binary units, the vectors of physical dimensions of

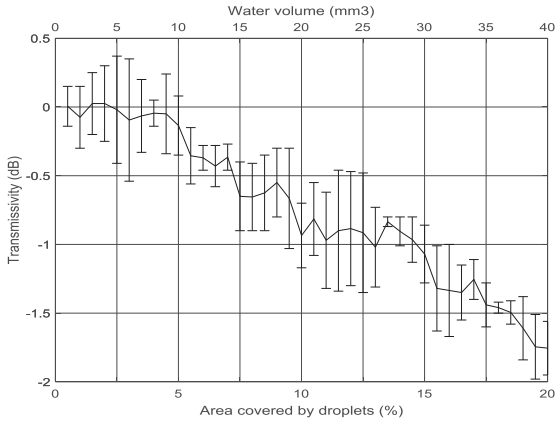

Fig. 15. Transmissivity through randomly distributed droplets at 150 GHz.

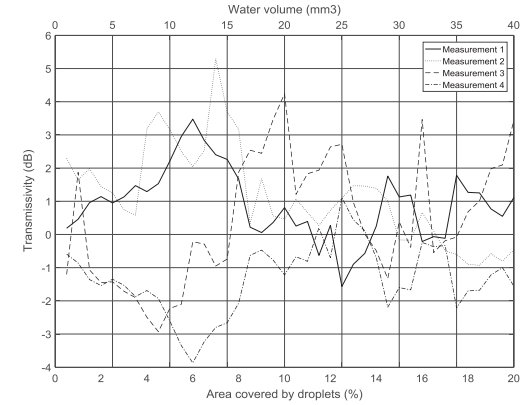

(a)

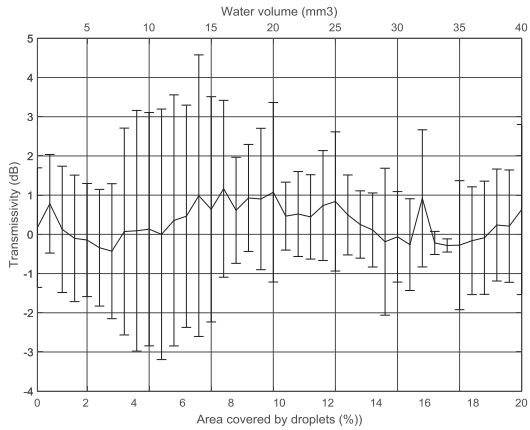

(b)

Fig. 16. Transmissivity through pure water droplet screen at 300 GHz. (a) Measured transmissivity (b) average transmissivity.

gaps and droplet diameters are calculated. Average droplet size versus average spacing between droplets has been plotted in Fig. 13. This graph shows that the average spacing varies more than the average droplet size. Whereas droplets diameter varies from 0.4 to 1.1 mm, the spacing varies between 4 and 10 mm. By generating the histogram of droplet and gap sizes, we found that they fit log-normal distribution and shown in Fig. 14. Table II illustrates the range of size variations calculated from the produced droplet screens. An important parameter is the average

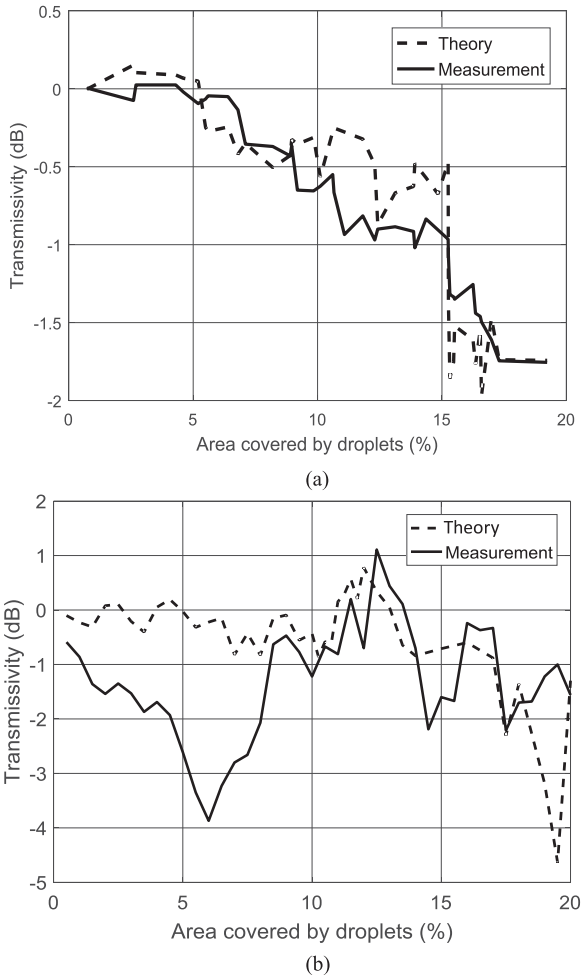

Fig. 17. Theoretical model and measurement results of transmissivity through water droplet screen (a) at 150 GHz and (b) at 300 GHz.

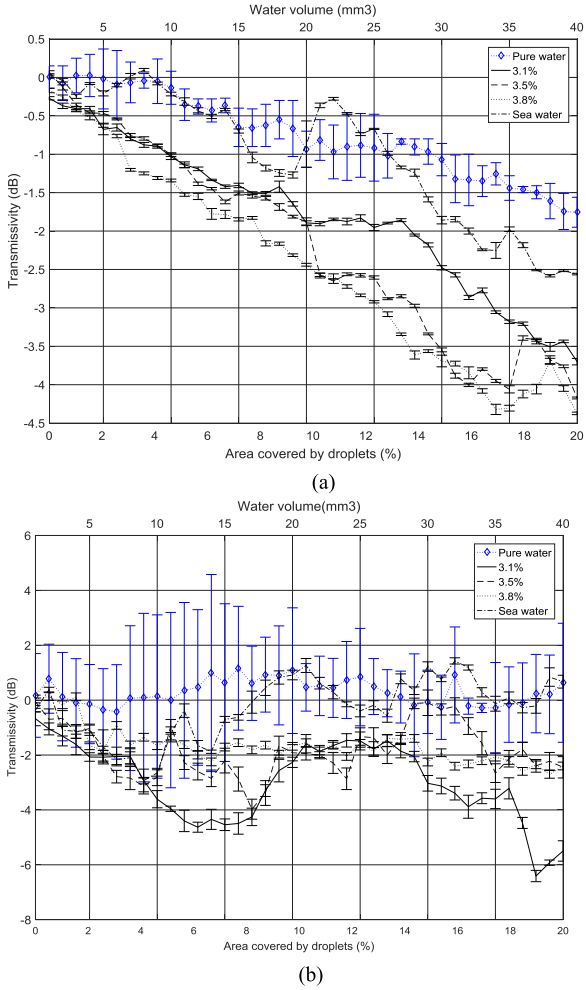

Fig. 18. Measured transmissivity through randomly distributed contaminated water droplets with salt at 23 °C (a) at 150 GHz and (b) at 300 GHz.

gap size, which is 7.4 mm. This dimension for the gaps has different implications on the effect of transmissivity through screens of water droplets at the two target low-THz frequencies. The average spacing of 7.4 mm between droplets is approximately 3.5λ at 150 GHz and 7λ at 300 GHz. As discussed in Section II, the expected trend for the transmissivity at 150 GHz would be a consistent decrease (as electrical dimensions of gaps are less than 4λ) and the transmissivity to be close to 0 dB at 300 GHz, as it is larger than 4λ.

C. Measurement Results

The measured results reported in this section are the transmissivity through randomly distributed droplets.

1) Pure Water: The graph in Fig. 15 shows the plot of transmissivity versus area covered by pure (deionized) water droplets (%) at 150 GHz. The results show that the transmissivity decreases with increasing water coverage on the droplet screen, as predicted by the theory. The transmissivity of –2 dB is measured when 20% of the screen is covered by droplets.

The results of transmissivity through four different pure water droplet screens at 300 GHz are shown in Fig. 16(a). These plots show that the transmissivity varies around 0 dB as predicted, with occasional enhancements of up to 5 dB and lowest transmissivity of –4 dB. The graph in Fig. 16(b) shows an average transmissivity of about 0 dB over the whole range of water volume deposited on the radome (20% of the area) with an overall RMS less than ±3 dB.

For one of the realizations at each frequency, the water droplet screens have been captured using a camera and translated to a matrix of 1 and 0 s. Each element of this matrix has an area of 0.0029 mm^2. The dimensions of the gaps, the distance between the center of the gaps and the source point, and the distance between the center of each gaps and the observation point were calculated and substituted in (10) to calculate the transmissivity through each specific droplet screen.

The theoretical model and measurement results are plotted together in Fig. 17 at 150 and 300 GHz. Fig. 17(a) shows a reasonably good agreement between the measurement results and the model at 150 GHz. A reasonable agreement between measurement and theory is achieved at 300 GHz for area covered by droplets more than 10%. The discrepancy for area coverage of less than 10% can be traced down to errors in the construction

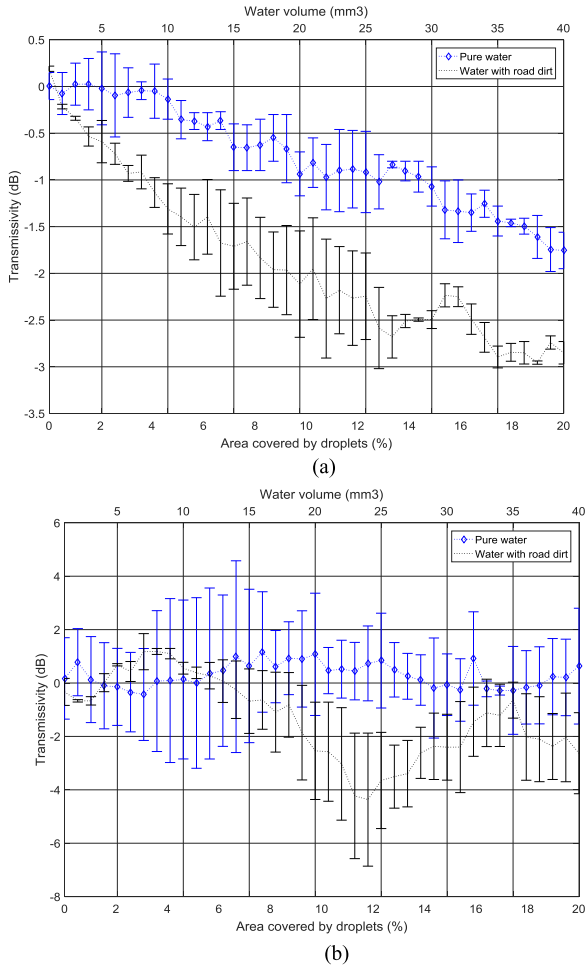

Fig. 19. Measured transmissivity through randomly distributed contaminated water droplets with road dirt at 23 °C (a) at 150 GHz (b) at 300 GHz.

of the input matrix to the theoretical model, as the captured photograph was unable to resolve a significant number of the smallest droplets. For area covered by droplets less than 10%, a significant number of small droplets are formed, whereas for higher volumes most of the small droplets coalesce together and form bigger droplets. The small captured droplet sizes are about 0.06 mm, which corresponds to about 0.1λ at 150 GHz and 0.2λ at 300 GHz. The effect of inaccurate modeling of these small droplets is more pronounced when the wavelength is shorter.

2) Water Contaminated With Salt: The droplet screen experiment has been replicated with salty water in the manner explained in the previous section. The transmissivity through a droplet screen of salty water with salinity of 3.1%, 3.5%, and 3.8% as well as actual seawater has been measured. The results for both frequencies are plotted in Fig. 18. The measured transmissivity through distributed salty water droplets at both frequencies shows a similar trend as in the corresponding case of the pure water droplet screen. A decreasing trend in transmissivity with increasing water volume deposited is observed at 150 GHz. Salty water has lower transmissivity than pure water; also, higher salinity results in lower transmissivity. Seawater shows the most similar trend to pure water. Transmissivity at 300 GHz does not have clear trend as it is dependent on the distribution of the droplets on the screen. The difference value between the saline water produced in the laboratory and pure water can be explained by undissolved salt particles and small variations in salt concentration that causes different scattering performance than pure water. This difference is less visible in seawater.

3) Water Contaminated With Road Dirt: Transmissivity through randomly distributed droplets of water contaminated with road dirt have been measured at 150 and 300 GHz to simulate scenarios relevant to automotive radar. The transmissivity results for both frequencies are plotted in Fig. 19. As discussed before, a decreasing trend is expected for 150 GHz signal and a relatively flat trend with some occasional fluctuation is expected at 300 GHz. The difference in transmissivity through road dirt contaminated water and pure water droplets is due to large quantities of suspended particles (soil, dust, etc.), which result in different scattering performance.

IV. Conclusion

Measured and theoretical modeling results of the transmissivity through uniform thickness of water and randomly distributed water droplets at 150 and 300 GHz have been presented in this paper. Good agreement is found between the measured results for uniform thickness of water and a simple theoretical model based on the Fresnel theory of reflection and transmission. The measurement and simulation results confirmed the expected strong transmission loss due to the presence of uniform thickness of water. However, it is important to note that a uniform layer of water does not form in real-life scenarios. A more common occurrence in outdoor applications, which has been studied in this paper for the first time, is transmission through a radome partially obscured by randomly distributed water droplets. Simulation and measurement results have shown an interesting effect on wave propagation through water droplets on the radome, specifically that wave propagation at sufficiently short wavelengths does not degrade the performance of the radar sensors radomes significantly. This demonstrates the potential of using low-THz sensors for outdoor applications. Similar characterization of the transmissivity of various contaminants with different moisture level will be considered in future work.

References

[1] [Online]. Available: http://ec.europa.eu/transport/index_en.htm, Accessed on: Sep. 2016.
[2] P. Thomas, A. Morris, R. Talbot, and H. Fagerlind, "Identifying the cause of road crashes in Europe," in *Proc. 57th Conf. Ann. Adv. Autom. Med.*, Sep. 22–25, 2013, pp. 13–22.
[3] J. Wenger, "Automotive radar—Status and perspectives," in *Proc. IEEE Compound Semicond. Integr. Circuit Symp.*, Oct. 2005, pp. 21–25.
[4] R. H. Rasshofer and K. Gresser, "Automotive radar and lidar systems for next generation driver assistance functions," *Adv. Radio Sci.*, vol. 3, pp. 205–209, 2005.
[5] A. K. Panwar, A. Singh, A. Kumar, and H. Kim, "Terahetz imaging systems for biomedical application: Current status," *Int. J. Eng. Technol.*, vol. 13, pp. 33–39, Apr. 2013.
[6] R. Appleby and H. B. Wallace, "Standoff detection of weapons and contraband in the 100 GHz to 1 THz region," *IEEE Trans. Antennas Propag.*, vol. 55, no. 11, pp. 2944–2956, Nov. 2007.

[7] K. B. Cooper *et al.*, "THz imaging radar for standoff personnel screening," *IEEE Trans. THz Sci. Technol.*, vol. 1, no. 1, pp. 169–182, Sep. 2011.
[8] D. Jasteh, E.G. Hoare, M. Cherniakov, and M. Gashinova, "Experimental low-terahertz radar image analysis for automotive terrain sensing," *IEEE Geosci. Remote Sens. Lett.*, vol. 13, no. 4, pp. 490–494, Apr. 2016.
[9] J. A. Hejase, E. J. Rothwell, and P. Chahal, "A multiple angle method for THz time-domain material characterisation," *IEEE Trans. THz Sci. Technol.*, vol. 3, no. 5, pp. 656–665, Sep. 2013.
[10] R. Piesiewicz *et al.*, "Scattering analysis for the modeling of THz communication systems," *IEEE Trans. Antennas Propag.*, vol. 55, no. 11, pp. 3002–3009, Nov. 2007.
[11] R. Appleby and R. N. Anderton, "Millimeter-wave and submillimeter-wave imaging for security and surveillance," *Proc. IEEE*, vol. 95, no. 8, pp. 1683–1690, Aug. 2007.
[12] R. J. Hogan, D. Bouniol, D. N. Ladd, W. J. O'Connor, and A. J. Illingworth, "Absolute calibration of 94/95-GHz radars using rain," *J. Atmos. Ocean. Technol.*, vol. 20, no. 4, pp. 572–580, 2002.
[13] B. C. Blevis, "Losses due to rain on radomes and antenna reflecting surfaces," *IEEE Trans. Antennas Propag.*, vol. 13, no. 1, pp. 175–176, Jan. 1965.
[14] J. Anderson, "Measurements of 20-GHz transmission through a radome in rain," *IEEE Trans. Antennas Propag.*, vol. 23, no. 5, pp. 619–622, Sep. 1975.
[15] A. Arage, G. Kuehnle, and R. Jakoby, "Measurement of wet antenna effects on millimetre wave propagation," in *Proc. IEEE Conf. Radar*, Apr. 2006, pp. 24–27.
[16] D. Brissinger, G. Parent, P. Boulet, "Experimental study on radiation attenuation by a water film," *J. Quant. Spectrosc. Radiat. Transf.*, vol. 20, no. 4, pp. 160–168, 2014.
[17] S. K. A. Rahim, A. Y. Abdulrahman, T. A. Rahman, and M. R. Ul Islam, "Measurement of wet antenna losses on 26 GHz terrestrial microwave link in Malaysia," *Wireless Pers. Commun.*, vol. 64, no. 2, pp. 225–231, May 2012.
[18] F. Norouzian *et al.*, "Signal reduction due to radome contamination in low-THz automotive radar," in *Proc. 2016 IEEE Radar Conf.*, Philadelphia, PA, USA, 2016, pp. 1–4.
[19] W. H. Hayt and J. A. Buck, *Engineering Electromagnetics*, 6th ed. New York, NY, USA: McGraw-Hill, 2001
[20] M. Koeberg, C. C. Wu, D. Kim, and M. Bonn, "THz dielectric relaxation of Ionic liquid: Water mixtures," *Chem. Phys. Lett.*, vol. 439, pp. 60–64, 2007.
[21] A. Beneduci, "Which is the effective time scale of the fast Debye relaxation process in water?" *J. Mol. Liquids*, vol. 138, pp. 55–60, 2008.
[22] R. Buchner, J. Barthel, and J. Stauber, "The dielectric relaxation of water between 0 °C and 35 °C," *Chem. Phys. Lett.*, vol. 306, pp. 57–63, Jun. 1990.
[23] C. Ronne and S. R. Keiding, "Low frequency spectroscopy of liquid water using THz-time domain spectroscopy," *J. Mol. Liquids*, vol. 101, pp. 199–218, 2002.
[24] U. Kaatze, "Complex permittivity of water as a function of frequency and temperature," *J. Chem. Eng. Data*, vol. 34, no. 4, pp. 371–374, 1989.
[25] J. T. Kindt and C. A. Schmuttenmaer, "Far-infrared dielectric properties of polar liquids probed by femtosecond terahertz pulse spectroscopy," *J. Phys. Chem.*, vol. 100, pp. 10373–10379, 1996.
[26] T. Meissner and F. J. Wentz, "The complex dielectric constant of pure and sea water from microwave satellite observations," *IEEE Trans. Geosci. Remote Sens.*, vol. 42, no. 9, pp. 1836–1849, Sep. 2004.
[27] [Online]. Available: www.vivatech.biz, Accessed on: Mar. 2016.
[28] M. N. Afsar, J. R. Birch, R. N. Clarke, and G. W. Chantry, "The measurement of the properties of materials," *Proc. IEEE*, vol. 74, no. 1, pp. 183–199, Jan. 1986.
[29] A. Buis and P. Lynch, "Studying earth's salty seas from space," Nat. Aeronaut. Space Admin., Washington, DC, USA, Jun. 2011.
[30] W. Qiao, K. Yang, A. Thoma, and T. Dekorsy, "Dielectric relaxation of HCI and NaCI solutions investigated by Terahertz time-domain spectroscopy," *J. Infrared Millim. THz Waves*, vol. 33, pp. 1029–1038, 2012.
[31] N. Q. Vinh *et al.*, "High-precision gigahertz-to-terahertz spectroscopy of aqueous salt solution as a probe of the femtosecond-to-picosecond dynamics of liquid water," *J. Chem. Phys.*, vol. 142, 2015, Art. no. 164502.
[32] M. Kurri and A. Huuskonen, "Measurement of the transmission loss of a radome at different rain intensities," *J. Atmos. Ocean. Technol.*, vol. 25, pp. 1590–1599, Sep. 2008.
[33] R. Danzl, F. Helmli, and S. Scherer, "Focus variation— A robust technology for high resolution optical 3D surface metrology," *J. Mech. Eng.*, vol. 57, pp. 245–256, 2011.
[34] H. C. Van de Hulst, *Light Scattering by Small Particles*. New York, NY, USA: Dover, 1981.
[35] M. Born and E. Wolf, *Principles of Optics*, 7th ed. Cambridge, U.K.: Cambridge Univ. Press, 1999.

Fatemeh Norouzian received the Ph.D. degree in electronic and communication engineering from the University of Birmingham, Birmingham, U.K. in 2015.

After receiving the Ph.D. degree, she continued with the University of Birmingham, as a Research Fellow. Her current research focuses on propagation and scattering in random medium at low-THz frequency. Her research interests include low-THz technology for future road vehicles, electromagnetic theory and measurement, and propagation modeling.

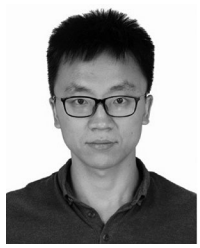

Rui Du is currently working toward the Ph.D. degree in information and communication engineering at Northwestern Polytechnical University, Xi'an, China.

He is a Visiting Ph.D. Student with the University of Birmingham, Birmingham, U.K. His research interests include propagation and scattering at low-THz frequencies, target identification and classification, and array signal processing.

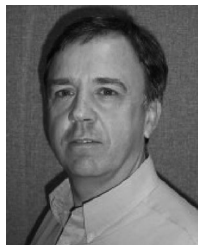

Edward G. Hoare (S'87–M'89–SM'99) received the Ph.D. degree working on over-the-horizon radar from the School of Electronic, Electrical and Computer Engineering, University of Birmingham, Birmingham, U.K.

He undertook an apprenticeship with The Royal Radar Establishment, College of Electronics, Malvern, U.K. and after a period of time in industry joined the University of Birmingham. Since then, he has been involved in teaching, design, and research into radar systems and antennas covering frequencies from 2 MHz to over 670 GHz including noncooperative bistatic radar, atmospheric radar acoustic sounding, automotive radar, and low-THz radar. Over the past 20 years, he has provided antenna and millimeter-wave radar consultancy to Jaguar Land Rover and Ford Motor Company. He holds a number of patents in automotive radar.

Dr. Hoare was a member of the European Automotive Radar Standards Group.

Peter Gardner received the B.A. degree in physics from the University of Oxford, Oxford, U.K., in 1980, and the M.Sc. and Ph.D. degrees in electrical engineering and electronics from the University of Manchester Institute of Science and Technology, Manchester, U.K., in 1990 and 1992, respectively.

He is a Professor of microwave engineering, the Head of the Department of Electronic, Electrical, and Systems Engineering, and the Head of the Communication and Sensing Research Group, University of Birmingham, Birmingham, U.K. He was appointed a Lecturer with the University of Birmingham in 1994 and became a Professor in 2015. His research interests include the theory, technology, and applications of the RF, microwave, millimeter-wave and THz bands.

Costas Constantinou was born in Famagusta, Cyprus, in 1964. He received the B.Eng. (Hons.) degree in electronic and communications engineering and Ph.D. degree in electronic and electrical engineering from the University of Birmingham, Birmingham, U.K., in 1987 and 1991, respectively.

In 1989, he joined the Faculty of the Department of Electronic, Electrical, and Systems Engineering, University of Birmingham, where he is currently the Chair for Communication Electrodynamics and the Head of the Antennas and Applied Electromagnetics Laboratory, Communications and Sensing Research Group. His research interests include optics, electromagnetic theory, electromagnetic scattering and diffraction, electromagnetic measurement, radiowave propagation modeling, mobile radio, and communications networks.

Mikhail Cherniakov received the Graduate degree from Moscow Technical University, Moscow, Russia, in 1974, the Ph.D. degree in 1980, and the D.Sc. degree in 1992.

He became a Full Professor in 1993. He is currently the Chair for Aerospace and Electronic Systems, University of Birmingham, Birmingham, U.K., with more than 40-year experience in the R&D of radar systems. In 1994, he was a Visiting Professor with the University of Cambridge, and in 1995, he joined The University of Queensland, Brisbane, QLD, Australia. In 2000, he joined the School of Electronic, Electrical, and Systems Engineering, University of Birmingham, where he founded the Microwave Integrated Systems Laboratory, which is the biggest radar research team in U.K. universities. He has authored/edited/co-authored 5 books and has more than 250 peer-reviewed publications. His research interests include bistatic and multistatic radar, radars with phased array, automotive and short range sensors.

Prof. Cherniakov was the recipient of Christian Hülsmeyer Award for his achievements in radar research and education in 2017.

Marina Gashinova received the M.Sc. degree in mathematics from Saint Petersburg State University, Saint Petersburg, Russia, in 1991, and the Ph.D. degree in physics and mathematics from Saint Petersburg Electrotechnical University, Saint Petersburg, Russia in 2003.

In 2006, she joined the Microwave Integrated System Laboratory, University of Birmingham, Birmingham, U.K., where she is currently a Senior Lecturer involved with radar and RF sensors, leading the research group on THz radar imaging and automotive sensors.